analytical chemistry

pubs.acs.org/ac Article

High Spatial Resolution MALDI Imaging Mass Spectrometry of Fresh-Frozen Bone

Christopher J. Good, Elizabeth K. Neumann, Casey E. Butrico, James E. Cassat, Richard M. Caprioli, and Jeffrey M. Spraggins*

Cite This: *Anal. Chem.* 2022, 94, 3165−3172 Read Online

ACCESS | Metrics & More | Article Recommendations | Supporting Information

ABSTRACT: Bone and bone marrow are vital to mammalian structure, movement, and immunity. These tissues are also commonly subjected to molecular alterations giving rise to debilitating diseases like rheumatoid arthritis and osteomyelitis. Technologies such as matrix-assisted laser desorption/ionization (MALDI) imaging mass spectrometry (IMS) facilitate the discovery of spatially resolved chemical information in biological tissue samples to help elucidate the complex molecular processes underlying pathology. Traditionally, preparation of osseous tissue for MALDI IMS has been difficult due to its mineralized composition and heterogeneous morphology, and compensation for these challenges with decalcification and fixation protocols can remove or delocalize molecular species. Here, sample preparation methods were advanced to enable multimodal MALDI IMS of undecalcified, fresh-frozen murine femurs, allowing the distribution of endogenous lipids to be linked to tissue structures and cell types. Adhesive-bound bone sections were mounted onto conductive glass slides with microscopy-compatible glue and freeze-dried to minimize artificial bone marrow damage. High spatial resolution (10 μm) MALDI IMS was employed to characterize lipid distributions, and use of complementary microscopy modalities aided tissue and cell assignments. For example, various phosphatidylcholines localize to the bone marrow, adipose tissue, marrow adipose tissue, and muscle. Further, sphingomyelin(42:1) was abundant in megakaryocytes, whereas sphingomyelin(42:2) was diminished in this cell type. These data reflect the vast molecular and cellular heterogeneity indicative of the bone marrow and the soft tissue surrounding the femur. Multimodal MALDI IMS has the potential to advance bone-related biomedical research by offering deep molecular coverage with spatial relevance in a preserved native bone microenvironment.

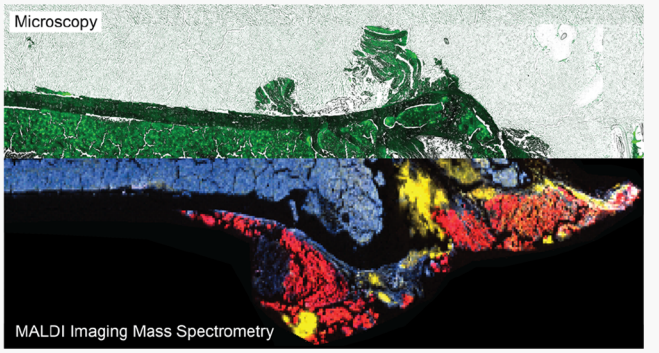

INTRODUCTION

Bones provide structural support, enable muscle-mediated mobility, and are responsible for regulating mineral homeostasis, acid−base physiology, and the hematopoietic stem cell niche.[1] Housed in the intramedullary cavity of long bones, bone marrow possesses extensive cellular and chemical heterogeneity due to hematopoiesis and helps in the development of adaptive and innate immunity. Bone marrow and its skeletal encasing can be compromised by a variety of disorders including those caused by autoinflammation,[2] bone remodeling imbalances,[3] nutritional deficiencies,[4] infection,[5] and cancer.[6] Approaches using cell culture, flow cytometry, immunohistochemistry, microcomputed tomography, and magnetic resonance imaging have contributed significantly to research on bone-associated diseases.[7−11] Matrix-assisted laser desorption/ionization (MALDI) imaging mass spectrometry (IMS) is an emerging technology that has the ability to advance our fundamental understanding of bone biology, especially under pathological conditions, by probing the molecular environment in the bone while preserving the native spatial context.

MALDI IMS offers spatially resolved, multi-omics data with high sensitivity and label-free chemical specificity.[12−15] In brief, laser irradiation is used to ionize endogenous molecules from a tissue surface producing mass spectra in an array of distinct x−y coordinates. The signal intensity of each detected molecule with a given mass-to-charge ratio (m/z) can be visualized as a heat map across this surface array. MALDI IMS of bone presents certain challenges resulting from the mineralized and vascularized nature of the tissue. Demineralization strategies have been used to remove the mineral content that can interfere with the detection of organic constituents.[16]

Received: October 24, 2021
Accepted: January 28, 2022
Published: February 9, 2022

https://doi.org/10.1021/acs.analchem.1c04604
Anal. Chem. 2022, 94, 3165−3172

However, these methods can lead to inconsistent preservation of tissue and loss of chemical integrity in terms of the native structure and distribution of biomolecules.[17,18] Formalin fixation maintains vascular and cellular structures in the bone marrow but results in removal, cross-linking, or delocalization of molecular species. Therefore, imaging of undecalcified and unfixed tissue is ideal, but extensive preparation is required to preserve the heterogeneous morphology of the cortical bone, trabecular bone, and bone marrow, all of which differ in porosity and density. Thus, only a handful of studies perform MALDI IMS of fresh-frozen osseous tissue as opposed to decalcified and/or fixed tissue.[19−22]

By preparing fresh-frozen murine tibias, Seeley et al.[19] reported on the application of MALDI IMS to a cancer model to identify differential expression of proteins within the skeletal environment following tumor growth. In another study, the effects of decalcification and fixation protocols on the molecular signal were evaluated in murine tibias.[20] Vandenbosch et al.[21] explored optimal embedding media and matrices for imaging lipids and metabolites in murine femurs. Further, MALDI-generated ion images of lipids were registered to elemental distributions in chicken phalanges.[22] In all reports, an adhesive was utilized to maintain the structural integrity of the fresh-frozen osseous tissue while cutting and mounting sections to the MALDI target substrate. A method established by T. Kawamoto and K. Kawamoto[23] is commonly implemented where the bone material is directly transferred from a tissue block to an adhesive film (Cryofilm) to prevent cryosectioning artifacts, such as cracks and folds in the tissue. While the results of these studies are encouraging, further investigation of strategies to improve lipid sensitivity and prevent artificial cracking of bone marrow tissue is required if high spatial resolution imaging modalities are to be employed.

Herein, we describe a method to prepare undecalcified, fresh-frozen murine femurs for high spatial resolution (10 μm) MALDI IMS and complementary microscopy. Bone sections bound to an adhesive film are mounted flat to MALDI-compatible surfaces by means of a liquid adhesive that possesses minimum interference for autofluorescence and bright-field microscopy and is electrically conductive. Artificial bone marrow damage is assessed for different sample thawing methods and matrix applications, and strategies to increase lipid signals are subsequently investigated. Although many lipid classes are detected in bone-associated tissues and cells, observed phosphatidylcholine (PC) and sphingomyelin (SM) distributions are highlighted. The protocol described herein addresses various challenges that have hindered previous methods for MALDI IMS of fresh-frozen bone tissue and enables high spatial resolution multimodal molecular imaging of this critical organ system.

METHODS

Chemicals. Acetone, acetonitrile, hematoxylin, eosin, carboxymethyl cellulose (CMC), and 1,5-diaminonapthalene (DAN, 97%, further purified by recrystallization) were purchased from Sigma-Aldrich (St. Louis, MO, USA). Ethanol, isopentane, isopropanol (IPA), gelatin, and the optimal cutting temperature (OCT) compound were purchased from Fisher Scientific (Pittsburgh, PA, USA). A Clearium mounting medium was purchased from Electron Microscopy Sciences (Hatfield, PA, USA).

Tissue Preparation. The right femurs of three 9 week-old female C57BL/6J mice (Jackson Laboratory, Bar Harbor, ME, USA) were removed and used for MALDI IMS experiments. Two weeks prior to removal, the mice underwent a procedure on the left leg as part of a separate study; the left femurs were directly inoculated with phosphate-buffered saline as detailed in a previously described murine osteomyelitis model.[10] All animal handling and experimental procedures were conducted in accordance with protocols approved by the Vanderbilt University Institutional Animal Care and Use Committee (IACUC).

Once dissected, femurs were immediately snap frozen over a dry ice-isopentane slurry and stored at −80 °C. Femurs were subsequently embedded in a warm aliquot of 5% CMC and 10% gelatin[24] that was concurrently snap frozen over dry ice-isopentane. Embedded femurs were mounted to a chuck using the OCT compound. Femurs were cryosectioned at 8 μm thickness using a DB80 HS microtome blade in a CM3050 S cryostat (Leica Biosystems, Wetzlar, Germany) set to −25 °C. Cryofilm 3C 16UF (SECTION-LAB, Hiroshima, Japan) was directly applied to the tissue block to assist in complete tissue transfer.[23] The Cryofilm-bound tissue was mounted flat onto glass slides (Fisher Scientific, Pittsburgh, PA, USA) or conductive indium tin oxide (ITO)-coated glass slides (Delta Technologies, Loveland, CO, USA) by means of ZIG 2 way glue (Kuretake Co, Nara, Japan), which was first utilized for mounting Cryofilm by Schaepe et al.[25] For preparations involving thaw-mounting, sections were removed from the cryostat to which heat was directly added followed by −80 °C storage until being brought to ∼22 °C (ambient temperature) in a desiccator. For preparations incorporating freeze-drying, sections were directly stored at −80 °C from the cryostat. Frozen sections were then placed in a glass apparatus surrounded by dry ice and kept under vacuum at ∼1 Torr for 8 h. The chamber was subjected to ambient temperatures for an additional hour. A 7811020 CentriVap Cold Trap (Labconco, Kansas City, MO, USA) was used to condense water vapor.

Autofluorescence Microscopy. An AxioScan.Z1 slide scanner (Carl Zeiss Microscopy GmbH, Oberkochen, Germany) was used for acquiring autofluorescence images using the EGFP (ex: 488 nm, em: 509 nm), DAPI (ex: 353 nm, em: 465 nm), and DsRed (ex: 545 nm, em: 572 nm) LEDs prior to MALDI IMS. A *z*-stack of five slices over a 35 μm range was acquired at every tile and merged to account for height differences between the bone marrow and cortical bone. After MALDI IMS acquisition, autofluorescence images were collected using EGFP and bright-field to visualize the MALDI burn patterns and progression of bone marrow cracks.

Matrix Application. For the spraying matrix, a robotic aerosol TM Sprayer (HTX Technologies, Chapel Hill, NC, USA) deposited a 10 mg/mL solution of DAN in 90% acetonitrile onto the sample. Pure acetonitrile flow and N_2 flow were set to 0.1 mL/min and 10 psi, respectively. The nozzle was heated to 75 °C and allowed to pass across the sample six times with a track spacing of 1.5 mm. The amount of deposited matrix per unit area was measured as 1.6 μg/mm^2. Alternatively, an in-house sublimation apparatus was used for matrix sublimation.[26,27] A solution of DAN in acetone (20 mg/mL × 3 mL) was uniformly dispersed on a heated surface and was sublimed at temperatures >130 °C for 10 min under 30 mTorr vacuum, which resulted in a uniform matrix layer (4.1 μg/mm^2) on the chilled sample. Following sublimation, the deposited matrix was recrystallized using a hydration chamber as described in a previous method.[28] In brief, samples were

https://doi.org/10.1021/acs.analchem.1c04604
Anal. Chem. 2022, 94, 3165−3172

mounted to a metal disc using thermally conductive copper tape (Electron Microscopy Sciences, Hatfield, PA, USA), primed in a 55 °C oven for 2 min, sealed in a Petri dish with 1 mL 5% IPA on filter paper,[29] heated at 55 °C for 30 or 90 s, and dried in a 55 °C oven for an additional 2 min.

MALDI Q-TOF IMS. A timsTOF fleX (Bruker Daltonics, Bremen, Germany) with a dual ESI-MALDI source was used to acquire all MALDI IMS data.[30] A SmartBeam 3D 10 kHz frequency tripled Nd:YAG laser (355 nm) was tuned to provide the optimal signal with the beam scan activated to produce a 16 μm × 16 μm footprint and 8 μm × 8 μm footprint for 20 and 10 μm spatial resolution imaging, respectively. The local laser power was set to 49 or 71% for 20 μm spatial resolution and decreased to 40% for 10 μm (attenuator offset: 0%). Shots remained consistent at 200 per pixel for all experiments. The additional height of the mount and Cryofilm was accounted for by a Galvo scanner offset focus adjustment. The MS was operated in qTOF mode with TIMS deactivated. ESI-L Tune Mix (Agilent Technologies, Santa Clara, CA, USA) was directly infused for mass calibration prior to data acquisition. Positive ion mode data were acquired from m/z 300 to 1500. Additional MS parameters are included in the Supporting Information (Table S1).

MALDI FT-ICR IMS. High-mass-resolution data were acquired on an FT-ICR MS system from a portion of thaw-mounted bone marrow to obtain high mass accuracy for lipid assignment. A 15T solariX FT-ICR mass spectrometer (Bruker Daltonics, Bremen, Germany) equipped with a Smartbeam II 2 kHz frequency tripled Nd:YAG laser (355 nm) was used. The laser was focused on tissue by adjusting the z-position of the MALDI plate. The laser power, shot count, and pixel size were set to 34%, 275, and 100 μm^2, respectively. The instrument was mass calibrated using red phosphorus followed by online lock mass calibration to $[PC(34:1) + H]^+$ (m/z 760.5851). Positive ion mode data were acquired from m/z 345 to 2000 with a time domain file size of 1M, which resulted in a mass resolving power of ∼140,000 at m/z 760.6. Additional MS parameters are included in the Supporting Information (Table S2).

Histology. Following post-IMS autofluorescence microscopy, DAN was removed with a pure ethanol wash for 2 min. The sample was stained with hematoxylin and eosin before a cover slip was mounted with a Clearium mounting medium. A bright-field microscopy z-stack image was collected at 20× magnification using the Zeiss AxioScan.Z1 slide scanner.

Data Analysis. All imaging data were visualized using SCiLS Lab Version 2021 (Bruker Daltonics, Bremen, Germany). Ion images were created using the hotspot removal function without normalization and denoising. With hotspot removal, the intensity scale bar is not given in a traditional 0−100% range but is rather set to an optimal range that is mathematically defined by the 99% quantile of the image. A larger scale typically correlates to a less abundant ion unless the range has been noted to be manually adjusted. Regions of interest were drawn around the bone marrow using inherent tissue contrast from ion images. These intramedullary cavity regions were used to compare signals between samples. All boxplots were derived from SCiLS by plotting an intensity value for each pixel. Mean intensity values were extracted from peaks in the mean spectrum of a given region. A peak list was generated and matched with lipids from the LIPIDMAPS database to identify intense ions based on mass accuracy with a <1 ppm mass error tolerance (Table S3).[31,32]

RESULTS AND DISCUSSION

Tissue Preparation for Multimodal Molecular Imaging. Cryofilm 3C 16UF maintained its adhesive properties at −25 °C (cryosectioning temperature) and enabled reproducible murine femur sections of 8 μm thickness (Figure 1A). Cryosectioning mineralized and unfixed bone without an adhesive led to tissue loss and distortion that is visible without magnification (Figure S1). For high spatial resolution analysis, it is imperative that the tissue maintains its structure to preserve the spatial accuracy of MALDI IMS data. After adhering the tissue section, single-sided Cryofilm was mounted flat onto a glass slide using an optically transparent glue that has minimal fluorescence interference at wavelengths used with DAPI, DsRed, and EGFP (Figure 1A). Substrate and adhesive transparency are required for multimodal imaging experiments where bright-field and fluorescence microscopy can be used to annotate the functional structures and cell types within the tissue. If the mount inherently produces a fluorescent background, then it would be more challenging to identify morphological structures without additional stains, many of which are incompatible with mass spectrometry analysis. Furthermore, a mount that minimizes air bubbles and promotes a level tissue surface is necessary for MALDI IMS to limit topographical changes that can lead to defocusing of the laser at the tissue surface. Overall, the mounting adhesive and Cryofilm are ideal for generating reproducible bone samples that are compatible with MALDI IMS and microscopy modalities.

Balancing Tissue Morphology and Signal When Thawing and Applying Matrix. Strategies to bring frozen femur sections to ambient temperatures (∼22 °C) were investigated (Figure 1B). A tradeoff arose between preserving bone marrow morphology and achieving adequate signal intensity of biomolecules. Tissue sections are thaw-mounted directly to the slide in traditional MALDI IMS experiments; however, thaw-mounting a femur section directly onto Cryofilm resulted in artificial bone marrow cracks as large as 75 μm wide (Figure S2). We hypothesize that the residual water content in this gelatinous soft tissue is responsible for artifact formation. Removing water content by lyophilization/freeze-drying yielded less pronounced cracks that are nearly indistinguishable by MALDI IMS at a 20 μm spatial resolution (Figure 1C), although cracks were still noticeable when using microscopy modalities. Previously, Saigusa et al.[33] reported an increase in the metabolite signal in rat brain that was thaw-mounted to Cryofilm compared to freeze-dried sections, and we observed the same trend for lipid signals in murine bone marrow (Figure 1B,C,E). After mounting the tissue onto a slide, the matrix was deposited using either a robotic aerosol sprayer or sublimation apparatus, and spraying resulted in an intensity increase for lipids such as $[PC(34:1) + H]^+$ (m/z 760.59, Figure 1D,E). The solvents used when depositing the matrix aid in the extraction of molecules from the tissue surface, which results in an enhanced signal. This is a phenomenon that does not occur with dry matrix applications like sublimation.

Following a closer examination of tissue morphology, solvent exposure from spraying matrix contributed to additional bone marrow damage or cracks (Figure 2). Minor artifacts manifested from the freeze-drying process, likely due

https://doi.org/10.1021/acs.analchem.1c04604
Anal. Chem. 2022, 94, 3165−3172

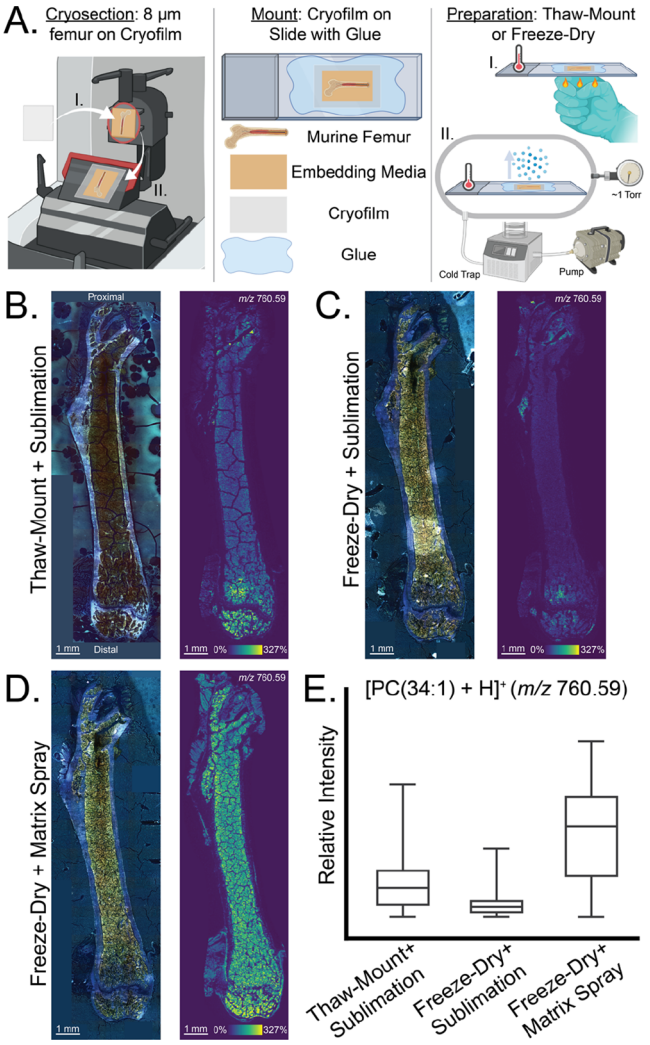

Figure 1. Methods for preparing adhesive-bound, fresh-frozen femur sections lead to differences in bone marrow morphology and signal intensity of biomolecules. (A) Overview of sample preparation that is compatible with MALDI IMS and microscopy modalities: cryosectioning (I. apply film, II. cut section), mounting, and preparing sections (I. thaw-mount, II. freeze-dry). (B–D) Merged channel autofluorescence images (left) and ion images of $[PC(34:1) + H]^+$ (m/z 760.59; right) highlight the morphological damage and lipid signal between thaw-mounting, freeze-drying, matrix sublimation, and matrix spraying. (B) Thaw-mounting and subliming matrix yield large bone marrow cracks. (C) Freeze-drying and subliming matrix result in less pronounced cracks but worse signals. (D) Freeze-drying and spraying matrix recover signals with an additional sacrifice to morphology. (E) Boxplots recapitulate intensity differences of $[PC(34:1) + H]^+$ (m/z 760.59) between sample preparation methods. Boxplots represent the range and interquartile range of a molecule's intensity values, which are derived from all pixels within a singular intramedullary cavity. These MALDI IMS data were collected in positive ion mode at a 20 μm spatial resolution. Ion images were not normalized for intensity comparisons between tissue sections.

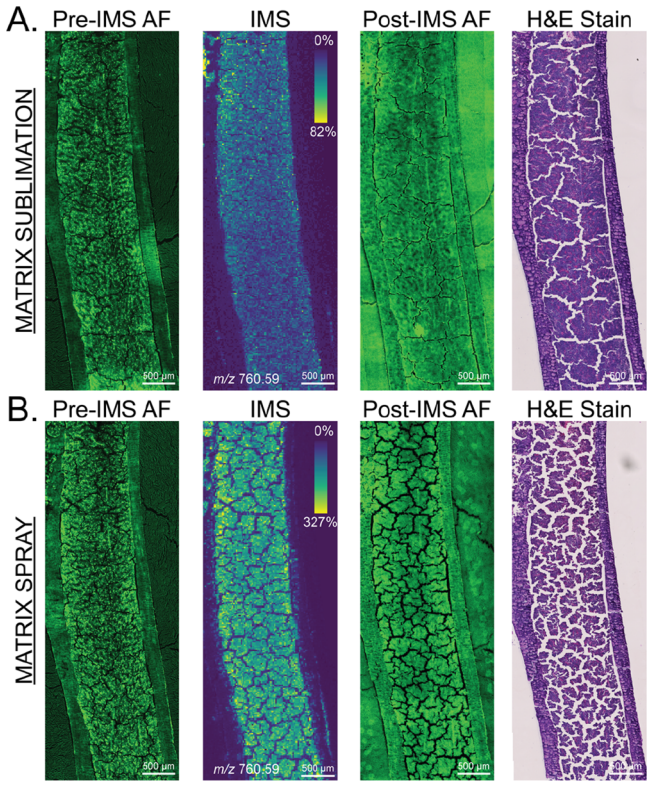

Figure 2. Spraying matrix generates more severe bone marrow artifacts that negatively affect MALDI IMS data and downstream microscopy. (A, B) Autofluorescence (EGFP, pre- and post-IMS), 20 μm spatial resolution ion images of $[PC(34:1) + H]^+$ (m/z 760.59), and H&E staining display the propagation of bone marrow cracks throughout an MALDI IMS experiment. Bone marrow cracks are less pronounced when the (A) matrix is sublimed compared to when the (B) matrix is sprayed. The intensity scale bar of the ion image in (A) was manually adjusted to help visualize cracks. The matrix layer appears in the post-IMS autofluorescence images. Ion images were not normalized.

to incomplete water removal from the tissue. These cracks appear in the pre-IMS images and are accentuated in the post-IMS images, regardless of the matrix application method (Figure 2A,B). In the post-IMS autofluorescence images, the matrix layer adds contrast to the artifacts and increases their visibility. Moreover, during H&E staining protocols, ethanol washing shrunk the bone marrow and exacerbated the cracks in the tissue. Bright-field microscopy also reveals bone marrow artifacts because the light source illuminates the sample through the backside of the slide. Nevertheless, tissue exposure to sublimed DAN and MALDI laser irradiation did not significantly alter tissue morphology (Figure 2A). This observation is confirmed in Figure 3C when comparing both pre- and post-IMS bright-field images and is consistent with the previous literature.[34] In contrast, sprayed DAN contributed to additional and more pronounced bone marrow cracks that compromised ion and histological images (Figure 2B). Aerosolized solvent exposure was the source of additional morphological damage, and thus sublimation was determined to be the optimal matrix application method.

Improving Lipid Signals with Matrix Recrystallization and Conductive Coatings. Freeze-drying femur sections and applying matrix by sublimation resulted in the least amount of bone marrow damage; however, the overall lipid signal was relatively low. Recrystallizing the matrix layer with 5% aqueous IPA improved the signal intensity of most lipid species in a time-dependent manner, including $[PC(34:1) + H]^+$ (m/z 760.59; Figure 3A,B). Improvement in signals was observed with as little as 30 s of recrystallization, and 90 s of exposure to IPA vapor yielded a 437% intensity increase for $[PC(34:1) + H]^+$ (m/z 760.59) with minimal molecular delocalization. This

https://doi.org/10.1021/acs.analchem.1c04604
Anal. Chem. 2022, 94, 3165−3172

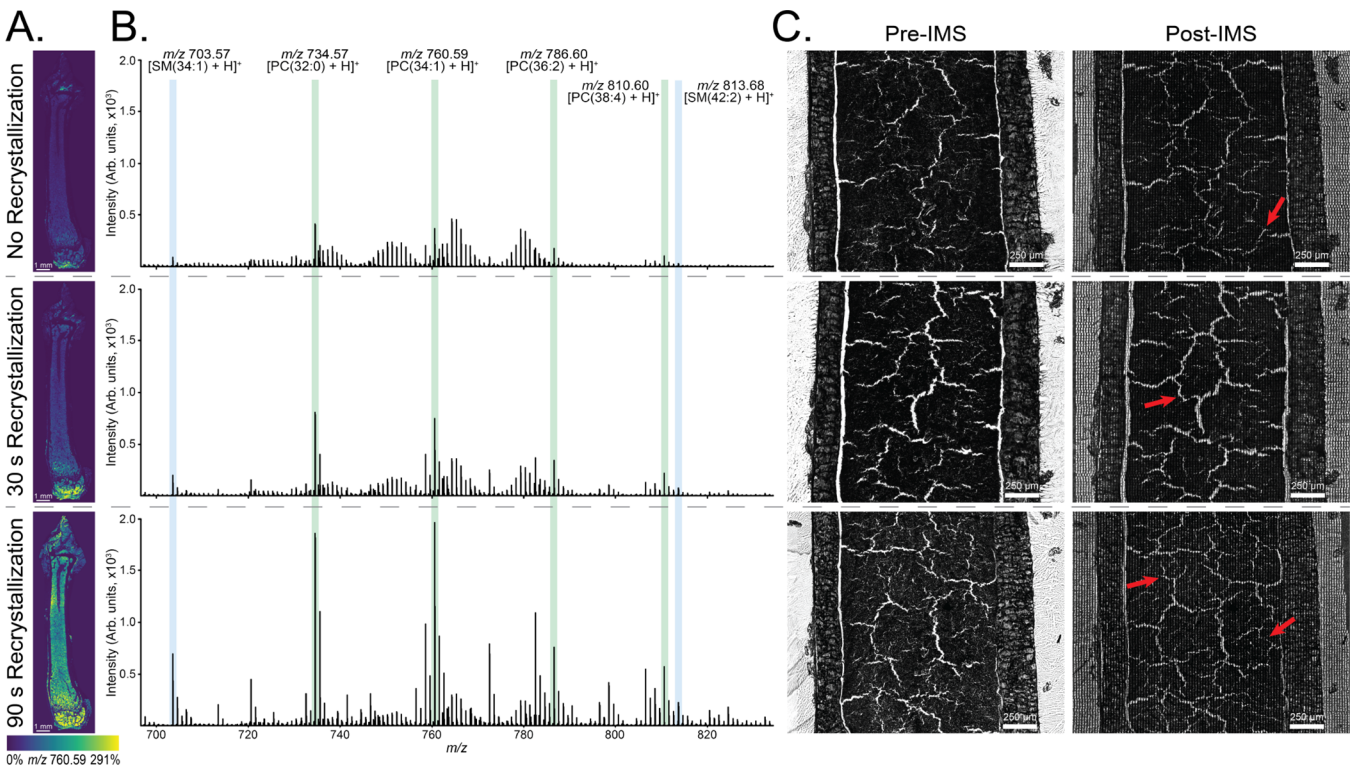

Figure 3. Recrystallizing the deposited matrix increases lipid signals and does not significantly contribute to bone marrow damage. (A–C) Images and spectra are aligned across; the top represents no recrystallization, the middle represents 30 s of recrystallization, and the bottom represents 90 s of recrystallization. (A) 20 μm spatial resolution ion images of $[PC(34:1) + H]^+$ (m/z 760.59) highlight the improvement in signal for full femur sections as the recrystallization time increases. (B) Unnormalized mean spectra show an intensity increase for various PCs (green) and SMs (blue). (C) Red arrows in the post-IMS bright-field images indicate minor cracks that manifest from matrix deposition, recrystallization (if applicable), and MALDI IMS.

trend was consistent regardless of lipid class, degree of unsaturation, or acyl chain length as observed with $[PC(32:0) + H]^+$ (m/z 734.57), $[PC(36:2) + H]^+$ (m/z 786.60), $[PC(38:4) + H]^+$ (m/z 810.60), $[PC(34:1) + H]^+$ (m/z 760.59), $[SM(34:1) + H]^+$ (m/z 703.57), and $[SM(42:2) + H]^+$ (m/z 813.68; Figure 3B). These protonated lipids are only a representative subset of the detectable lipidome in positive ion mode, and preliminary results suggest that sample preparation methods are compatible with negative ion mode (Figure S3). Following the recrystallization procedure, additional bone marrow damage did not appear to be significant (Figure 3C). There was evidence of the formation of <10 μm cracks; however, the number and severity of newly formed cracks did not correlate with different recrystallization time points. We anticipate that a further increase in recrystallization time will improve the signal but at the cost of spatial resolution due to molecular diffusion and morphological damage. Optimization of these time points may be required when analyzing different organ systems. Overall, recrystallizing DAN on freeze-dried femur sections enables ample lipid signals without further compromising bone marrow morphology.

Cryofilm 3C 16UF was predicted to be nonconductive since it comprises a polyvinylidene chloride film and acrylic resin cryoglue.[35] For MALDI IMS, a charged surface enhances ion acceleration and dissipates charge accumulation on the tissue surface, which improves the ionization and signal. Therefore, alternative conductive adhesives have been explored for imaging mass spectrometry.[21,33] Interestingly, a notable intensity increase was discovered when the Cryofilm-bound tissue was mounted onto an ITO-coated glass slide in lieu of a glass slide (Figure 4). All m/z features detected in the intramedullary cavity, including those identified as PCs and SMs, exemplified a greater signal when mounted to a conductive surface. This trend held true for lower abundant lipids like $[SM(42:2) + H]^+$ (m/z 813.68), where a 34.9% intensity increase was still observed. The combination of the mounting adhesive and Cryofilm is sufficiently conductive to permit the advantage gained from an ITO coating.

Molecular Mapping of Tissue Structures and Immune Cells in Bone Tissue. The sample preparation methods discussed thus far were leveraged to visualize and define endogenous lipid distributions in macroscopic soft tissues within and surrounding the intramedullary cavity of undecalcified bone (Figure 5). Pre-IMS autofluorescence and post-IMS histological staining were used to define functional tissue units, such as cortical bone, trabecular bone, bone marrow, adipose tissue, and muscle. Lipids localized to most soft tissue structures, but some showed differential distributions based on the acyl chain length and degree of unsaturation. For example, $[PC(32:0) + H]^+$ (m/z 734.57) was the most abundant lipid in the bone marrow, while $[PC(36:2) + H]^+$ (m/z 786.60) and $[PC(38:6) + H]^+$ (m/z 806.57) were primarily distributed in contiguous adipose tissue and muscle tissue, respectively. There was no identifiable lipid signal from the cortical or trabecular bone regions, which is consistent with a previously published study using DAN.[21]

Adipocytes comprise a central mass of stored triglycerides surrounded by a phospholipid membrane. In addition to surrounding the femur as white adipose tissue, adipocytes

https://doi.org/10.1021/acs.analchem.1c04604
Anal. Chem. 2022, 94, 3165−3172

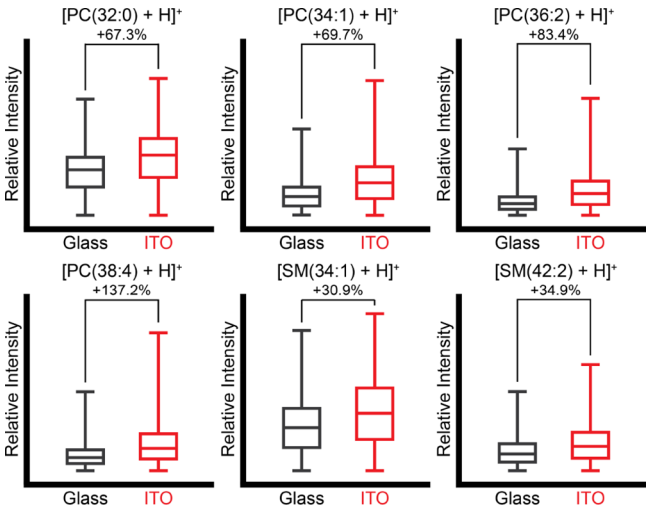

Figure 4. Cryofilm-bound tissue mounted to an ITO-coated glass slide provides an additional improvement in signal for all PCs and SMs regardless of their native abundances in tissue. Boxplots represent the range and interquartile range of a molecule's intensity values, which are derived from all pixels within a singular intramedullary cavity. Please note that the intensity scaling is different for each boxplot, and the intensity increase percentages were calculated from the unnormalized mean intensity values for each region. The deposited matrix was recrystallized for 30 s, and MALDI IMS data were collected at a 20 μm spatial resolution.

constitute a portion of bone marrow cellular content called marrow adipose tissue.[36] Colocalization of $[PC(32:0) + H]^+$ (m/z 734.57) and $[PC(36:2) + H]^+$ (m/z 786.60) was observed at the distal end of the femur. These lipid signatures provide a molecular and visual representation of marrow adipose tissue, which is consistent with previous findings. The marrow adipose tissue volume in long bones of 4−12 week-old C57BL/6J mice has been determined to be greater in distal regions compared to proximal regions.[37] Others have also identified PC(36:2) in white and brown murine adipose tissues,[38] both of which possess analogous characteristics of marrow adipose tissue.[39]

Our new sample preparation and MALDI IMS technologies enabled imaging of femur sections at a 10 μm spatial resolution (Figure S4). Even though bone marrow artifacts are accentuated in the higher spatial resolution images, lipid profiles from individual cells and vasculature were able to be detected with this method (Figure 6). Microscopy highlighted the location of a blood vessel and hematopoietic cells in the bone marrow, and histological analysis suggested the identity of these large cells as megakaryocytes (Figure 6A). Megakaryocytes generate platelets and have diverse cytoplasmic and membrane lipid content that consist of both phosphatidylcholines and sphingomyelins.[40] As differentiated megakaryocytes mature, their cell diameter expands and the nucleus becomes multilobed.[41] We have identified megakaryocytes with different diameters (~20−30 μm) and nuclear configurations that exemplify variations in maturity (Figure S5). Regardless of maturity, megakaryocytes were observed to have greater abundances of some sphingomyelins relative to surrounding cell types (Figure 6B). For instance, $[SM(42:1) + H]^+$ (m/z 815.70) and $[SM(40:1) + H]^+$ (m/z 787.67) possessed higher abundances within the megakaryocytes. In contrast, $[SM(42:2) + H]^+$ (m/z 813.68) differs by only one

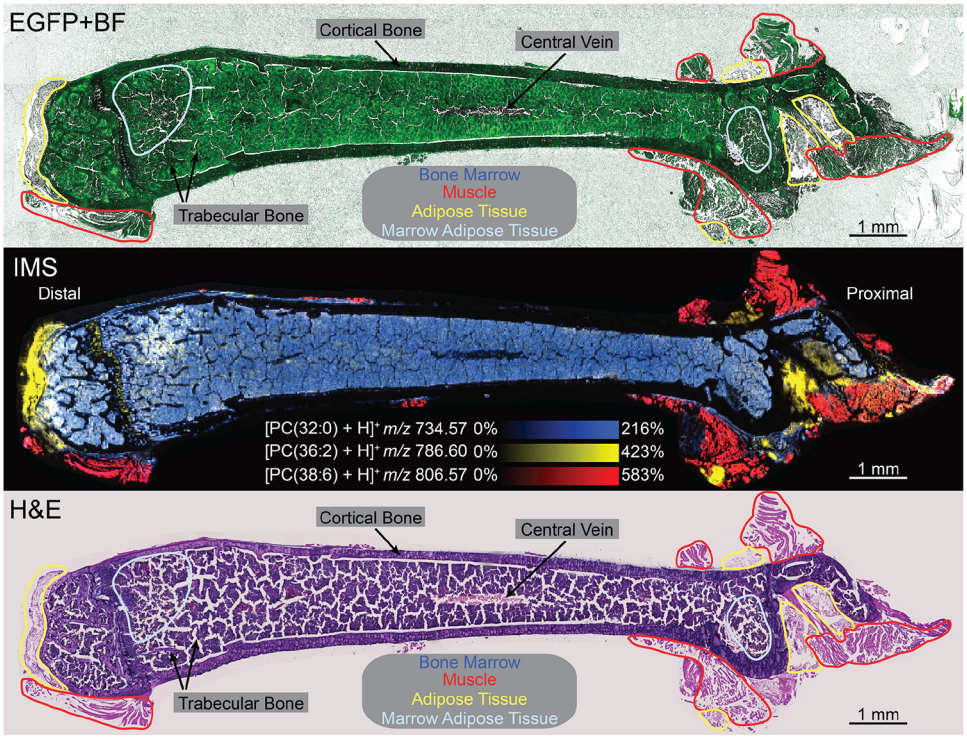

Figure 5. Sample preparation methods enable visualization of lipid distributions in various tissue structures defined by histology. $[PC(32:0) + H]^+$ (m/z 734.57), $[PC(36:2) + H]^+$ (m/z 786.60), and $[PC(38:6) + H]^+$ (m/z 806.57) localize to the bone marrow, adipose tissue, and muscle, respectively. Pre-IMS autofluorescence (EGFP) with bright-field (BF) microscopy and post-IMS histological staining (H&E) aid in tissue and cell assignments. The following ions are listed in order of decreasing mean intensity values: m/z 734.57, m/z 786.60, m/z 806.57. MALDI IMS data were collected at a 20 μm spatial resolution, and ion images were not normalized.

https://doi.org/10.1021/acs.analchem.1c04604
Anal. Chem. 2022, 94, 3165−3172

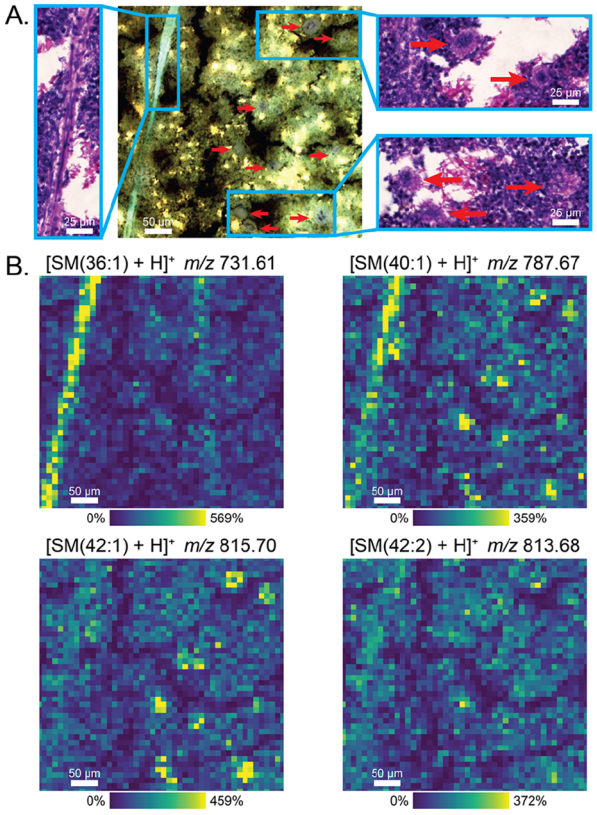

Figure 6. Sphingomyelins localize to microscopic vascular structures and individual megakaryocytes in the bone marrow. (A) Merged channel autofluorescence and enlarged H&E stain images reveal a blood vessel and multiple megakaryocytes (red arrows). (B) $[SM(36:1) + H]^+$ (m/z 731.61) and $[SM(40:1) + H]^+$ (m/z 787.67) localize to the blood vessel. The latter also localizes to individual megakaryocytes in addition to $[SM(42:1) + H]^+$ (m/z 815.70). An extra degree of unsaturation decreases the presence of the 42-carbon chain SM within the cells. MALDI IMS data were collected at a 10 μm spatial resolution, and ion images were not normalized.

degree of unsaturation and exhibited a decrease in abundance within these cells. High spatial resolution imaging also uncovered specific lipids that localized to blood vessels within the bone, such as $[SM(40:1) + H]^+$ (m/z 787.67) and $[SM(36:1) + H]^+$ (m/z 731.61). These data suggest some degree of lipid preservation following the complex molecular process of thrombopoiesis within the bone marrow.

CONCLUSIONS

The advanced sample preparation methods described herein allowed us to perform multimodal molecular imaging of undecalcified, fresh-frozen murine femurs at a cellular spatial resolution. To achieve optimal signal intensity of biomolecules while preserving unfixed bone marrow morphology, Cryofilm-assisted cryosections were mounted flat onto ITO-coated glass slides via an adhesive and subsequently freeze-dried. The matrix sublimation and recrystallization processes do not exacerbate bone marrow damage and yield ample lipid signals. We were able to identify lipids that localize to the bone marrow, adipose tissue, marrow adipose tissue, muscle, blood vessels, and megakaryocytes. We also determined that the chain length and degree of unsaturation of sphingomyelins dictate their abundances within megakaryocytes. Tissue and cell assignments were made using complementary microscopy modalities, which emphasizes the importance of developing methods that are compatible with these imaging technologies. We believe that this multimodal MALDI IMS workflow can be leveraged for research of metabolic processes associated with marrow adipose tissue, physiological mechanisms like thrombopoiesis, and molecular modifications resulting from pathological conditions within the bone microenvironment.

ASSOCIATED CONTENT

Supporting Information

The Supporting Information is available free of charge at https://pubs.acs.org/doi/10.1021/acs.analchem.1c04604.

Additional MS parameters, accurate mass lipid identifications, measurements of bone marrow cracks, negative ion mode data, megakaryocyte images, and data replicates (PDF)

AUTHOR INFORMATION

Corresponding Author

Jeffrey M. Spraggins − *Mass Spectrometry Research Center, Department of Chemistry, Department of Biochemistry, and Department of Cell and Developmental Biology, Vanderbilt University, Nashville, Tennessee 37235, United States;* orcid.org/0000-0001-9198-5498; Email: jeff.spraggins@vanderbilt.edu

Authors

Christopher J. Good − *Mass Spectrometry Research Center and Department of Chemistry, Vanderbilt University, Nashville, Tennessee 37235, United States;* orcid.org/0000-0002-4900-274X

Elizabeth K. Neumann − *Mass Spectrometry Research Center and Department of Biochemistry, Vanderbilt University, Nashville, Tennessee 37235, United States;* orcid.org/0000-0002-6078-3321

Casey E. Butrico − *Department of Pathology, Microbiology, and Immunology, Vanderbilt University Medical Center, Nashville, Tennessee 37232, United States*

James E. Cassat − *Department of Pathology, Microbiology, and Immunology, Department of Pediatrics, and Vanderbilt Institute for Infection, Immunology, and Inflammation, Vanderbilt University Medical Center, Nashville, Tennessee 37232, United States; Department of Biomedical Engineering, Vanderbilt University, Nashville, Tennessee 37235, United States*

Richard M. Caprioli − *Mass Spectrometry Research Center, Department of Chemistry, Department of Biochemistry, Department of Medicine, and Department of Pharmacology, Vanderbilt University, Nashville, Tennessee 37235, United States*

Complete contact information is available at: https://pubs.acs.org/10.1021/acs.analchem.1c04604

Author Contributions

The manuscript was written through contributions of all authors. All authors have given approval to the final version of the manuscript.

Notes

The authors declare no competing financial interest.

https://doi.org/10.1021/acs.analchem.1c04604
Anal. Chem. 2022, 94, 3165−3172

■ ACKNOWLEDGMENTS

The authors would like to thank Dr. Eric Spivey and Dr. David Anderson for developing and troubleshooting the in-house sublimation apparatus. Figure 1,A was created with BioRender.com (BQ231UWMH9). Support was provided by the NIH National Institute of Allergy and Infectious Diseases (R01 AI145992 awarded to J.M.S. and J.E.C.), the NIH Shared Instrumentation Grant Program (S10 OD012359 awarded to R.M.C.), and the NSF Major Research Instrument Program (CBET 1828299 awarded to J.M.S. and R.M.C.). C.J.G. and C.E.B. are supported by the NIH National Institute of Allergy and Infectious Diseases (T32 AI112541). E.K.N. is supported by the NIH National Institute of Environmental Health Sciences (T32 ES007028). J.E.C. is also supported by the NIH National Institute of Allergy and Infectious Diseases (R01 AI132560) and a Burroughs Welcome Fund Career Award for Medical Scientists.

■ REFERENCES

(1) Clarke, B. *Clin. J. Am. Soc. Nephrol.* **2008**, *3*, S131−S139.
(2) Ferguson, P. J.; El-Shanti, H. I. *Curr. Opin. Rheumatol.* **2007**, *19*, 492−498.
(3) Feng, X.; McDonald, J. M. *Annu. Rev. Pathol.: Mech. Dis.* **2011**, *6*, 121−145.
(4) Karpouzos, A.; Diamantis, E.; Farmaki, P.; Savvanis, S.; Troupis, T. *J. Osteoporosis* **2017**, *2017*, 4218472.
(5) Lew, D. P.; Waldvogel, F. A. *Lancet* **2004**, *364*, 369−379.
(6) Rajkumar, S. V.; Kumar, S. *Mayo Clin. Proc.* **2016**, *91*, 101−119.
(7) Kuca-Warnawin, E.; Kurowska, W.; Prochorec-Sobieszek, M.; Radzikowska, A.; Burakowski, T.; Skalska, U.; Massalska, M.; Plebańczyk, M.; Małdyk-Nowakowska, B.; Słowińska, I.; Gasik, R.; Maśliński, W. *Arthritis Res. Ther.* **2017**, *19*, 274.
(8) Aalbers, A. M.; van den Heuvel-Eibrink, M. M.; Baumann, I.; Dworzak, M.; Hasle, H.; Locatelli, F.; de Moerloose, B.; Schmugge, M.; Mejstrikova, E.; Nováková, M.; Zecca, M.; Zwaan, C. M.; te Marvelde, J. G.; Langerak, A. W.; van Dongen, J. J. M.; Pieters, R.; Niemeyer, C. M.; van der Velden, V. H. J. *Haematologica* **2015**, *100*, 315−323.
(9) Bussard, K. M.; Okita, N.; Sharkey, N.; Neuberger, T.; Webb, A.; Mastro, A. M. *Clin. Exp. Metastasis* **2010**, *27*, 331−340.
(10) Cassat, J. E.; Hammer, N. D.; Campbell, J. P.; Benson, M. A.; Perrien, D. S.; Mrak, L. N.; Smeltzer, M. S.; Torres, V. J.; Skaar, E. P. *Cell Host Microbe* **2013**, *13*, 759−772.
(11) Daffner, R.; Lupetin, A.; Dash, N.; Deeb, Z.; Sefczek, R.; Schapiro, R. *Am. J. Roentgenol.* **1986**, *146*, 353−358.
(12) Caprioli, R. M.; Farmer, T. B.; Gile, J. *Anal. Chem.* **1997**, *69*, 4751−4760.
(13) Stoeckli, M.; Chaurand, P.; Hallahan, D. E.; Caprioli, R. M. *Nat. Med.* **2001**, *7*, 493−496.
(14) McDonnell, L. A.; Heeren, R. M. A. *Mass Spectrom. Rev.* **2007**, *26*, 606−643.
(15) Karlsson, O.; Hanrieder, J. *Arch. Toxicol.* **2017**, *91*, 2283−2294.
(16) Hirano, H.; Masaki, N.; Hayasaka, T.; Watanabe, Y.; Masumoto, K.; Nagata, T.; Katou, F.; Setou, M. *Anal. Bioanal. Chem.* **2014**, *406*, 1355−1363.
(17) Hosoya, A.; Hoshi, K.; Sahara, N.; Ninomiya, T.; Akahane, S.; Kawamoto, T.; Ozawa, H. *Histochem. Cell Biol.* **2005**, *123*, 639−646.
(18) Liu, H.; Zhu, R.; Liu, C.; Ma, R.; Wang, L.; Chen, B.; Li, L.; Niu, J.; Zhao, D.; Mo, F.; Fu, M.; Brömme, D.; Zhang, D.; Gao, S. *BioMed Res. Int.* **2017**, *2017*, No. e9050754.
(19) Seeley, E. H.; Wilson, K. J.; Yankeelov, T. E.; Johnson, R. W.; Gore, J. C.; Caprioli, R. M.; Matrisian, L. M.; Sterling, J. A. *Bone* **2014**, *61*, 208−216.
(20) Fujino, Y.; Minamizaki, T.; Yoshioka, H.; Okada, M.; Yoshiko, Y. *Bone Rep.* **2016**, *5*, 280−285.
(21) Vandenbosch, M.; Nauta, S. P.; Svirkova, A.; Poeze, M.; Heeren, R. M. A.; Siegel, T. P.; Cuypers, E.; Marchetti-Deschmann, M. *Anal. Bioanal. Chem.* **2021**, 2683.
(22) Svirkova, A.; Turyanskaya, A.; Perneczky, L.; Streli, C.; Marchetti-Deschmann, M. *Analyst* **2018**, *143*, 2587−2595.
(23) Kawamoto, T.; Kawamoto, K. Preparation of Thin Frozen Sections from Nonfixed and Undecalcified Hard Tissues Using Kawamot's Film Method (2012). In *Skeletal Development and Repair: Methods and Protocols*; Hilton, M. J., Ed.; Methods in Molecular Biology; Humana Press: Totowa, NJ, *2014*; pp. 149−164, DOI: 10.1007/978-1-62703-989-5_11.
(24) Nelson, K. A.; Daniels, G. J.; Fournie, J. W.; Hemmer, M. J. *J Biomol Tech* **2013**, *24*, 119−127.
(25) Schaepe, K.; Bhandari, D. R.; Werner, J.; Henss, A.; Pirkl, A.; Kleine-Boymann, M.; Rohnke, M.; Wenisch, S.; Neumann, E.; Janek, J.; Spengler, B. *Anal. Chem.* **2018**, *90*, 8856.
(26) Hankin, J. A.; Barkley, R. M.; Murphy, R. C. *J. Am. Soc. Mass Spectrom.* **2007**, *18*, 1646−1652.
(27) Thomas, A.; Charbonneau, J. L.; Fournaise, E.; Chaurand, P. *Anal. Chem.* **2012**, *84*, 2048−2054.
(28) Yang, J.; Caprioli, R. M. *Anal. Chem.* **2011**, *83*, 5728−5734.
(29) Dueñas, M. E.; Carlucci, L.; Lee, Y. J. *J. Am. Soc. Mass Spectrom.* **2016**, *27*, 1575−1578.
(30) Spraggins, J. M.; Djambazova, K. V.; Rivera, E. S.; Migas, L. G.; Neumann, E. K.; Fuetterer, A.; Suetering, J.; Goedecke, N.; Ly, A.; Van de Plas, R.; Caprioli, R. M. *Anal. Chem.* **2019**, *91*, 14552−14560.
(31) Sud, M.; Fahy, E.; Cotter, D.; Brown, A.; Dennis, E. A.; Glass, C. K.; Merrill, A. H.; Murphy, R. C.; Raetz, C. R. H.; Russell, D. W.; Subramaniam, S. *Nucleic Acids Res.* **2007**, *35*, D527−D532.
(32) Liebisch, G.; Fahy, E.; Aoki, J.; Dennis, E. A.; Durand, T.; Ejsing, C. S.; Fedorova, M.; Feussner, I.; Griffiths, W. J.; Köfeler, H.; Merrill, A. H.; Murphy, R. C.; O'Donnell, V. B.; Oskolkova, O.; Subramaniam, S.; Wakelam, M. J. O.; Spener, F. *J. Lipid Res.* **2020**, *61*, 1539−1555.
(33) Saigusa, D.; Saito, R.; Kawamoto, K.; Uruno, A.; Kano, K.; Aoki, J.; Yamamoto, M.; Kawamoto, T. *Anal. Chem.* **2019**, *91*, 8979−8986.
(34) Neumann, E. K.; Comi, T. J.; Rubakhin, S. S.; Sweedler, J. V. *Am. Ethnol.* **2019**, *131*, 5971−5975.
(35) Ticha, P.; Pilawski, I.; Yuan, X.; Pan, J.; Tulu, U. S.; Coyac, B. R.; Hoffmann, W.; Helms, J. A. *Sci. Rep.* **2020**, *10*, 19510.
(36) Li, Y.; Meng, Y.; Yu, X. *Front. Endocrinol.* **2019**, *10*, 69.
(37) Scheller, E. L.; Doucette, C. R.; Learman, B. S.; Cawthorn, W. P.; Khandaker, S.; Schell, B.; Wu, B.; Ding, S.-Y.; Bredella, M. A.; Fazeli, P. K.; Khoury, B.; Jepsen, K. J.; Pilch, P. F.; Klibanski, A.; Rosen, C. J.; MacDougald, O. A. *Nat. Commun.* **2015**, *6*, 7808.
(38) Hoene, M.; Li, J.; Häring, H.-U.; Weigert, C.; Xu, G.; Lehmann, R. *Biochim. et Biophys. Acta, Mol.Cell Biol. Lipids* **2014**, *1841*, 1563−1570.
(39) Krings, A.; Rahman, S.; Huang, S.; Lu, Y.; Czernik, P. J.; Lecka-Czernik, B. *Bone* **2012**, *50*, 546−552.
(40) Schick, B. P.; Schick, P. K.; Chase, P. R. *Biochim. Biophys. Acta* **1981**, *663*, 239−248.
(41) Long, M.; Williams, N. *Blood* **1981**, *58*, 1032−1039.

https://doi.org/10.1021/acs.analchem.1c04604
Anal. Chem. 2022, 94, 3165−3172